Generalized Newtonian fluid flow in porous media

Christopher A. Bowers* and Cass T. Miller
Department of Environmental Sciences and Engineering, University of North Carolina at Chapel Hill, North Carolina 27599, USA

(Received 22 November 2019; accepted 15 November 2021; published 6 December 2021)

Single-fluid-phase porous medium systems are typically modeled at an averaged length scale termed the macroscale, and Darcy's law is typically relied upon as an approximation of the momentum equation under Stokes flow conditions. Standard approaches for modeling macroscale single-fluid-phase flow of generalized Newtonian fluids (GNFs) extend the standard Newtonian model based upon Darcy's law using an effective viscosity and assuming that the intrinsic permeability is invariant with respect to fluid properties. This approach results in a need to perform an experiment for a non-Newtonian fluid, the introduction of effective parameters that are not tied to known microscale physics, and uncertainty regarding the dependencies of the fitted empirical parameter on system properties. We use the thermodynamically constrained averaging theory (TCAT) to examine the formulation and closure of a macroscale model for GNF flow that is consistent with microscale conservation principles and the second law of thermodynamics. A direct connection between microscale and macroscale quantities is used to formulate an expression for interphase momentum transfer for GNF flow in porous medium systems. Darcy's law is shown to approximate momentum transfer from the fluid phase to the solid phase. Momentum transfer is found to depend on the viscosity at the solid surface, which is only invariant for Newtonian flow. TCAT is used to derive a macroscale equation for the hydraulic resistance based on accessible fluid and solid properties. This hydraulic resistance may be used in the same way that hydraulic conductivity is typically used to model flow at the macroscale, and it includes parameters that can be calculated *a priori*, without the need to carry out microscale simulations, or experiments, for any GNF. The TCAT approach is validated for four model isotropic and anisotropic media and five Cross-model fluids. The traditional shift factor and effective viscosity are related to the newly derived TCAT model, shedding new light on this common empirical approach. The results from this work form a basis for the modeling of GNF flow in porous medium systems under Stokes flow, which is predictive given the rheological properties of the GNF and the resistance observed for Newtonian flow.

DOI: 10.1103/PhysRevFluids.6.123302

I. INTRODUCTION

Non-Newtonian fluids do not follow Newton's law of viscosity, which is written in scalar form as

$$\tau_w = \hat{\mu}_w \dot{\gamma}_w, \tag{1}$$

where τ_w is the shear stress, $\hat{\mu}_w$ is the dynamic viscosity of the fluid that is independent of $\dot{\gamma}_w$, $\dot{\gamma}_w$ is the shear rate, subscripts indicate that this expression is written at the microscale, and w is a phase index. The viscosity of non-Newtonian fluids may be dependent on the shear rate, time history of

*bowersca@live.unc.edu

the shear rate, and may exhibit time-dependence, as well as being impacted by typical temperature and pressure effects [1–4]. Generalized Newtonian fluids (GNFs) have a dynamic viscosity that is dependent on the shear rate of the fluid, but shear history and rate effects are assumed to be unimportant [1,4].

Several different rheological models have been used to describe GNFs, including power-law models, the Ellis model, the Carreau model, and the Cross model [1–5]. Power-law models are often used due to their relative simplicity, but they have been found to be ineffective for most fluids [6–8]. Four parameter models, such as the Cross and Carreau models, have been found to describe many fluids of interest [1,4,5,9–11]. The Cross model is a common model used to describe GNFs, and it may be written as

$$\hat{\mu}_w(\dot{\gamma}) = \hat{\mu}_{w\infty} + \frac{\hat{\mu}_{w0} - \hat{\mu}_{w\infty}}{1 + (m\dot{\gamma}_w)^n}, \tag{2}$$

where $\hat{\mu}_{w\infty}$ is the infinite shear dynamic viscosity, $\hat{\mu}_{w0}$ is the zero shear limit of dynamic viscosity, m is a measure of intermolecular attractive forces, and n is a non-Newtonian behavior index [5]. Equation (2) illustrates the nonlinear relationship between the dynamic viscosity and the shear rate as well as asymptotic behavior reducing to Newtonian flow at both low and high shear rates. It may be observed, as is typical of GNFs in general, that history effects and dynamic effects are absent from the formulation [9].

There are many processes that have been modeled as GNFs flowing in porous medium systems, including biofluidic [12–16], geophysical [17–24], and subsurface processes such as hydraulic fracturing and enhanced oil recovery [10,25–31]. The complexity of GNF mechanics has led to a reliance on phenomenological approaches that extend approaches for modeling Newtonian fluid flow through porous media to GNFs [1,4,11,32–36].

A complication that exists in modeling GNF flow through porous media is the lack of a clear, first-principles understanding of how to represent the nonlinear rheological behavior in a macroscale model of fluid flow through a porous medium, which has a complicated pore morphology and topology and a distribution of shear rates that vary in space and time [37–39]. The shift-factor approach is often used to describe empirically such flows [10,11,30,40,41]. The shift-factor approach is applied as follows: (1) an experiment for a Newtonian fluid is performed to determine the intrinsic permeabilty, $\hat{\kappa}^w$, which is assumed constant and independent of the fluid properties; (2) an experiment is performed for a medium of concern for the GNF composition of concern at a representative Stokes flow rate; (3) an effective viscosity, $\mu_{\text{eff}}^{\overline{\overline{w}}}$, is computed from the GNF experiment by assuming that Darcy's law applies [10,11,30,40–50]; (4) a GNF rheological model is assumed to apply at not only the microscale but also the macroscale, allowing for the determination of an effective shear rate, $\dot{\gamma}_{\text{eff}}^{\overline{\overline{w}}}$, that corresponds to the observed $\mu_{\text{eff}}^{\overline{\overline{w}}}$; and (5) the linear empirical relation

$$\dot{\gamma}_{\text{eff}}^{\overline{\overline{w}}} = \hat{\alpha}\frac{q^{\overline{\overline{w}}}}{\sqrt{\epsilon^{\overline{\overline{w}}}\hat{\kappa}^w}} \tag{3}$$

is used to approximate $\dot{\gamma}_{\text{eff}}^{\overline{\overline{w}}}$ as a linear function of $q^{\overline{\overline{w}}}$, the magnitude of the Darcy velocity, where $\epsilon^{\overline{\overline{w}}}$ is the porosity and $\hat{\alpha}$ is the shift factor. This approach thus extends the experimental results to all Stokes flow rates without a need to examine other flow rates.

The shift-factor approach has been developed as an empirical approach without theoretical understanding of the link between the microscale and the macroscale [10,11,45,46,51]. There is confusion as to what $\mu_{\text{eff}}^{\overline{\overline{w}}}$ represents, with some suggesting that it represents the dynamic viscosity at the fluid-solid interface [40,42], that it is the average dynamic viscosity throughout the fluid [3,30,49], that it is a "fictitious" dynamic viscosity [10,41,45], or that it is a "macroscopic" dynamic viscosity [46]. A desirable, but so far unavailable, alternative to the shift factor approach is a method that is theoretically based and relates the microscale rheology to the observed macroscale behavior,

TABLE I. Fluid parameters used in cases (1) through (4).

Parameter	Fluid 1	Fluid 2	Fluid 3	Fluid 4	Fluid 5
$\hat{\mu}_0$ (Pa s)	1.35×10^{-1}	1.35×10^{0}	1.35×10^{-1}	1.35×10^{-1}	1.35×10^{-1}
$\hat{\mu}_\infty$ (Pa s)	3.04×10^{-4}	3.04×10^{-4}	3.04×10^{-4}	3.04×10^{-4}	3.04×10^{-4}
m (s)	4.48×10^{-2}	4.48×10^{-2}	4.48×10^{0}	4.48×10^{-2}	4.48×10^{4}
n	6.85×10^{-1}	6.85×10^{-1}	6.85×10^{-1}	3.00×10^{-1}	6.85×10^{-1}
ρ^w (kg/m^3)	1.00×10^{3}	1.00×10^{3}	1.00×10^{3}	1.00×10^{3}	1.00×10^{3}

does not include ill-defined effective quantities, is predictive in nature by not requiring porous medium GNF flow experiments, and applies not only to isotropic media but also anisotropic media.

The terminology of length scales is inconsistent in the porous medium physics literature. To set the terminology used herein, we will rely on two scales, the microscale, or pore scale, and the macroscale, or porous medium continuum scale. The microscale is a scale at which the laws of continuum mechanics are applicable and the distribution of all phases is resolved in space and time. The macroscale is a scale where a point represents a centroid of an averaging region containing all phases in the vicinity of the point. The macroscale is the scale at which most field applications must be described because of computational limitations. There have been several successful attempts to derive the equations of flow by averaging to the macroscale from the microscale [52–57], and even some attempts when the fluid is non-Newtonian [45,46,58]. However, it is usually the case that the hydraulic conductivity of the system is what is derived by averaging, and it is assumed that this hydraulic conductivity may be decomposed into an intrinsic permeability and a fluid viscosity after averaging. Even in the case where it is acknowledged that a non-Newtonian viscosity may enter averaging [53], or that the actual permeability may be different than the intrinsic permeability [45,46], a precise link between microscale and macroscale properties of interest has not been conclusively established for GNF flow.

The thermodynamically constrained averaging theory (TCAT) is a model building approach that can be used to derive macroscale models based upon microscale principles [57,59,60]. TCAT has been used to derive model hierarchies for a wide variety of systems including single-fluid porous medium systems [59–63], two-fluid porous medium systems [60,64–66], sediment transport in surface waters [67], and tumor growth [68–70]. Advantages of utilizing the TCAT approach include the ability to use previously derived results to develop new macroscale models, and that all macroscale variables are explicitly defined in terms of averaged microscale variables. TCAT methods have not been used to formulate macroscale models for any type of non-Newtonian fluid flow in porous medium systems.

The goal of this paper is to develop and evaluate a new macroscale theory for Stokes flow of GNFs in a single-fluid porous medium that is consistent with microscale conservation and thermodynamic principles. The specific objectives of this work are: (1) to adapt an existing macroscale model hierarchy for single-fluid-phase flow to GNF flow; (2) to derive a macroscale model of Stokes flow for a commonly encountered class of GNFs; (3) to evaluate and validate the resultant model by comparison to ideal systems; and (4) to use the new model to advance understanding of traditional empirical approaches.

II. METHODS

Microscale simulations of GNF flow were carried out to validate the macroscale theory derived below. Four different media were simulated: a set of slits; a set of spheres arranged in a body-centered cubic (BCC) arrangement; polydisperse randomly packed spheres; and a body-centered ellipsoid (BCE) arrangement in which the principal directions of the ellipsoids were aligned with the unit vectors defining the Cartesian coordinate system. The Cross model rheological parameters

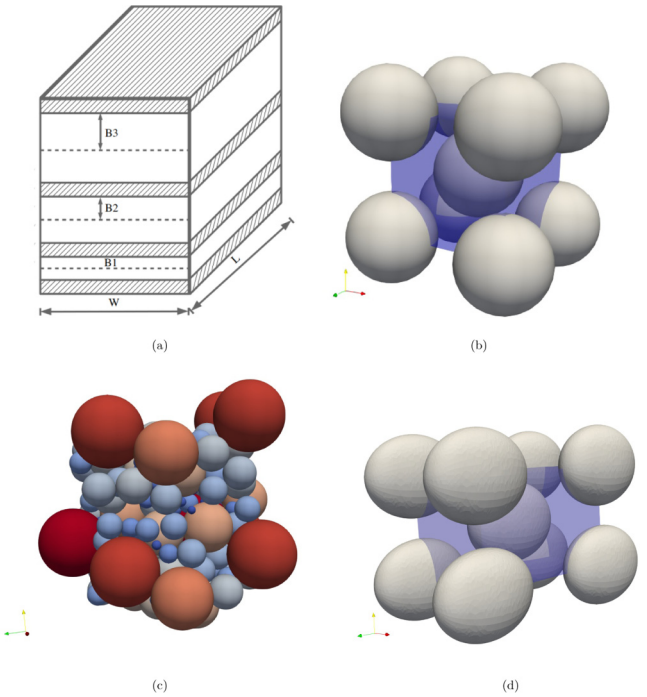

FIG. 1. Geometries used include: (a) a set of parallel slits; (b) a BCC array of spheres with the blue box representing the domain; (c) a polydisperse, randomly packed set of spheres; and (d) a BCE array of ellipsoids with the blue box representing the domain.

of the GNFs used for simulation are listed in Table I. The media are each described below, followed by the methods used for microscale simulation of the flow.

A representation of the four different media is shown in Fig. 1. Parallel slits were selected as a case for which an analytical solution exists. The BCC medium was selected as a model isotropic unit cell. The packed set of spheres represents a stochastic medium with a more complicated pore morphology and topology than the BCC case. The ellipsoid medium was selected as a model anisotropic unit cell.

For the parallel slit medium, three slits were arranged as shown in Fig. 1(a) with identical Dirichlet pressure conditions set at the inlet and outlet face for each slit and medium parameters given in Table II. The inlet of the medium was the face shown coming out of the page in Fig. 1(a), while the outlet was opposite of the inlet face.

The sphere centers of the BCC medium were located at the vertices of the cubic domain, with one sphere center located at the center of the domain, and the radii of all spheres were identical. The BCC medium was generated with periodic boundaries in all dimensions. Table III provides

TABLE II. Parallel slit domain description.

Parameter	Slit 1	Slit 2	Slit 3
Half-height B (m)	5.0×10^{-4}	1.0×10^{-3}	1.5×10^{-3}
Length (m)	1.0×10^{-2}	1.0×10^{-2}	1.0×10^{-2}
Width (m)	4.0×10^{-3}	4.0×10^{-3}	4.0×10^{-3}
Porosity ϵ	1.0×10^{0}	1.0×10^{0}	1.0×10^{0}

TABLE III. BCC and cubic packed sphere domain description.

Parameter	BCC	Packed Spheres
Number of Spheres	2	100
Domain Length (m)	1.00×10^{-3}	1.00×10^{-3}
Porosity (m^3/m^3)	5.82×10^{-1}	3.94×10^{-1}
Mean Radius (m)	3.68×10^{-4}	8.29×10^{-5}
Log Normal Radius Variance	0.00×10^{0}	4.00×10^{-1}
Number of Background Cells	200^3	400^3

additional details for the BCC system. Flow through the BCC medium was driven by an imposed body force on the fluid phase.

A standard method was used to generate a random distribution of nonoverlapping spheres with log-normally distributed radii [71]. The log-normal variance was selected to be large enough to provide a range of radii and hence a more complicated pore morphology and topology than the BCC medium. Additionally, this medium was generated to investigate a system that has a variety of significant length scales, with the largest sphere radius being 2.7×10^{-4}, and the smallest being 1.7×10^{-5}. The packed spheres were generated with fully periodic boundaries. System parameters for the random sphere pack case are detailed in Table III. Flow through this medium was driven by an imposed body force, with the boundary conditions in all dimensions being periodic.

A set of identical ellipsoids was arranged to yield a simple, anisotropic unit cell. The ellipsoid centers of the BCE medium were located at the vertices of the domain with one ellipsoid center located at the center of the domain. An STL file of the medium was generated using the open-source 3D parametric modeler FreeCAD [72]. The BCE medium was generated with fully periodic boundaries. The implicit equation of an ellipsoid is

$$\frac{x^2}{a^2} + \frac{y^2}{b^2} + \frac{z^2}{c^2} = 1, \tag{4}$$

where a, b, and c are scaling factors for the principal semiaxes of the ellipsoid that were aligned with the Cartesian coordinate system. Details for the BCE system are given in Table IV. Flow through the BCE medium was driven by an imposed body force on the fluid phase.

The flow rate through the parallel slits was calculated for each individual slit using an analytical solution derived for Cross model fluids [9]. The microscale shear rate and the dynamic viscosity were calculated within each slit using the Cross model and the known shear stress [1,9].

Microscale simulations for GNF flow through the BCC, packed sphere, and BCE cases were performed using the simpleFOAM solution package within OpenFOAM [73,74], while microscale averaging to the macroscale was carried out using Paraview [75]. SimpleFOAM solves the incompressible mass and momentum balance equations

$$\boldsymbol{\nabla} \cdot \mathbf{v}_w = 0, \tag{5}$$

$$\boldsymbol{\nabla} \cdot (\mathbf{v}_w \mathbf{v}_w) - \boldsymbol{\nabla} \cdot \boldsymbol{\tau}_w = -\boldsymbol{\nabla} p_w + \mathbf{S}, \tag{6}$$

TABLE IV. BCE system description.

Parameter	x	y	z
Domain Length (m)	1.00×10^{-3}	1.00×10^{-3}	1.50×10^{-3}
Scaling Factors (a, b, c) (m)	5.00×10^{-4}	2.50×10^{-4}	4.00×10^{-4}
Number of Background Cells	200	200	300

where $\mathbf{v}_w$ is velocity, $\boldsymbol{\tau}_w$ is the viscous stress tensor, p_w is the microscale fluid pressure, and $\mathbf{S}$ is a momentum source term. The viscous stress tensor for an incompressible GNF is

$$\boldsymbol{\tau}_w = 2\hat{\mu}_w \mathbf{d}_w, \tag{7}$$

where $\mathbf{d}_w$ is the rate of strain tensor defined as

$$\mathbf{d}_w = \tfrac{1}{2}[\nabla \mathbf{v}_w + (\nabla \mathbf{v}_w)^{\mathrm{T}}] \,. \tag{8}$$

The shear rate is calculated by

$$\dot{\gamma}_w = \sqrt{2\mathbf{d}_w : \mathbf{d}_w} \,. \tag{9}$$

Flow was driven by imposing a body force $\mathbf{S}$. For body-force driven flow all boundaries were periodic.

Microscale meshing of each of the systems was carried out using built in utilities in OpenFOAM [74]. The BCC, packed spheres, and BCE cases were all meshed using near-solid refinement, which has been found to be useful in other porous medium studies [76]. In all cases, the size of the mesh was selected such that computational error would be insignificant compared to the orders of magnitude of changes exhibited for the resistance to flow exhibited by GNFs flowing through the media considered over the range of velocities examined. Simulations were run using meshes of increasing refinement to determine an adequate mesh size, with successive meshes doubling in size in each dimension. Adequate refinement was determined when the relative difference between the flow resistance in successive levels of refinement was less than 1%. This implies that the numerical results for flow resistance are accurate to on the order of a couple percent in a relative error sense. The number of background cells used to mesh each system is listed in Tables III and IV.

III. THEORY

A. Framework

TCAT has been used to formulate a macroscale model hierarchy for single-fluid-phase flow through a porous medium [59,60]. This general model hierarchy can be used to formulate closed models of varying sophistication for a wide range of systems, including nonisothermal systems, systems with complex solid behavior, both Stokes and turbulent flows, and both Newtonian and GNF flows. While the framework is in place for the development of such models, work to date has considered only relatively simple systems consisting of Stokes flow of Newtonian fluids through systems with simple solid properties.

The framework consists of a simplified entropy inequality (SEI) that relates the sum of fluxes and forces for dissipative processes to the entropy production rate of the system, and a full set of macroscale conservation of mass, momentum, and energy equations. The formulation also includes precise descriptions of all macroscale variables in terms of averages of microscale variables, including expressions for the inter-entity exchange of conserved quantities. This explicit connection between the microscale and the macroscale provides a means to evaluate model approximations and to use averaged microscale simulation, or experimental, results to evaluate and validate a TCAT model. TCAT models are guided by closure approximations that are consistent with the second law of thermodynamics.

We use this framework to formulate a model for GNF flow of a single fluid through porous media. We will apply the following secondary restrictions to the general SEI [60]: (1) the system is isothermal; (2) the chemical composition of each entity is constant in space and time; (3) mass transfer does not occur between phases; (4) the interface between the fluid and solid is massless; (5) the interfacial tension between phases is constant; (6) flow is in the Stokes regime such that inertial terms in the momentum equation are insignificant; (7) the solid phase is incompressible, immobile, and has a constant orientation in space and time; (8) the porosity and specific interfacial area between the phases are constant in space and time; (9) the fluids are GNFs; and (10) the fluid

density is constant throughout the system at the microscale and macroscale. These conditions can be used to deduce a specific model instance from an available general model hierarchy [59,60]. The use of TCAT is a departure from extant phenomenological approaches that posit model forms directly at the macroscale [45,46]. In the sections that follow, we define the averaging process used, the conservation equations to be closed, the entropy inequality used to ensure consistency with the second law of thermodynamics, and the closure relations used to produce a closed model.

B. Averaging

Because the TCAT model includes averaged microscale quantities computed in different ways, some definitions are needed for clarity. For some quantity f that is averaged over the domain Ω_β, normalized by an integral over the domain Ω_γ, and weighted by W, the averaging operator is defined as [60,77]

$$\langle f\rangle_{\Omega_\beta,\Omega_\gamma,W} = \frac{\int_{\Omega_\beta} W f \, \mathrm{d}\mathfrak{r}}{\int_{\Omega_\gamma} W \, \mathrm{d}\mathfrak{r}} \, . \tag{10}$$

Various instances of Eq. (10) occur routinely, making it convenient to define a set of commonly occurring averaged forms. One common average is

$$f_\alpha^\beta = \langle f_\alpha\rangle_{\Omega_\beta,\Omega_\beta}, \tag{11}$$

where the subscript on f denotes the microscale entity (phase, or interface), the superscript denotes the entity over which averaging is performed, which is typically of one dimension lower than Ω_α, and the absence of W implies a unit value.

An intrinsic average is defined as

$$f^\alpha = \langle f_\alpha\rangle_{\Omega_\alpha,\Omega_\alpha}, \tag{12}$$

and a density-weighted average is defined as

$$f^{\overline{\alpha}} = \langle f_\alpha\rangle_{\Omega_\alpha,\Omega_\alpha,\rho_\alpha}, \tag{13}$$

where ρ_α is a mass density.

During averaging, some variables arise that do not fit one of the above special forms. Such macroscale averages are denoted with a double overbar and each occurrence is explicitly defined. A specific entity measure is such a quantity, and it is defined as

$$\epsilon^{\overline{\overline{\alpha}}} = \langle 1\rangle_{\Omega_\alpha,\Omega}, \tag{14}$$

where Ω is an averaging region that contains all entities.

C. Conservation equations

Mechanistic models of flow through porous media rely upon a set of conservation equations, and a set of closure relations to render the equations solvable. The relevant conservation equations include a conservation of mass equation for the fluid phase, which can be written after dropping the mass exchange term as specified in the secondary restrictions as [[60], Eq. (6.73)]

$$\frac{\partial(\epsilon^{\overline{\overline{w}}}\rho^w)}{\partial t} + \nabla\cdot(\epsilon^{\overline{\overline{w}}}\rho^w\mathbf{v}^{\overline{w}}) = 0, \tag{15}$$

and similarly a restricted conservation of momentum equation for the fluid phase is [[60], Eq. (6.92)]

$$\frac{\partial(\epsilon^{\overline{\overline{w}}}\rho^w\mathbf{v}^{\overline{w}})}{\partial t} + \nabla\cdot(\epsilon^{\overline{\overline{w}}}\rho^w\mathbf{v}^{\overline{w}}\mathbf{v}^{\overline{w}}) - \nabla\cdot(\epsilon^{\overline{\overline{w}}}\mathbf{t}^{\overline{\overline{w}}}) - \epsilon^{\overline{\overline{w}}}\rho^w\mathbf{g}^{\overline{w}} - \overset{s\to w}{\mathbf{T}} = \mathbf{0}, \tag{16}$$

where t is time, ρ^w is the macroscale fluid density, $\mathbf{v}^{\overline{w}}$ is the density-weighted macroscale velocity, $\mathbf{t}^{\overline{\overline{w}}}$ is the stress tensor, $\mathbf{g}^{\overline{w}}$ is the gravitational acceleration vector oriented positive in the negative z direction, $\overset{s\to w}{\mathbf{T}}$ is the rate of momentum density transfer from the solid phase to the fluid phase, s denotes the solid phase, and superscripts denote averaged macroscale variables.

D. Simplified entropy inequality and closure relations

Producing a solvable model requires a set of closure approximations for $\mathbf{t}^{\overline{\overline{w}}}$ and $\overset{s\to w}{\mathbf{T}}$, which can be deduced using an available simplified entropy inequality (SEI) [[60], Eq. (9.62)]. The standard TCAT approach for deriving an SEI is to derive a form for a general class of model to enable the use of this expression for any subset of the class of model considered; other approaches are possible [78]. Because general SEI expressions for the entropy production rate density are long, complicated equations, a useful strategy is to consider simple subsets of the most general case. Such a restricted SEI can be derived by applying the secondary restrictions noted in §III A to the general SEI yielding

$$\frac{1}{\theta}(\epsilon^{\overline{\overline{w}}}\mathbf{t}^{\overline{\overline{w}}}+\epsilon^{\overline{\overline{w}}}p^w\mathbf{I}):\mathbf{d}^{\overline{\overline{w}}}+\frac{1}{\theta}[\epsilon^{\overline{\overline{w}}}\nabla p^w-\epsilon^{\overline{\overline{w}}}\rho^w\nabla(\mu^{\overline{w}}+\psi^{\overline{w}})-\epsilon^{\overline{\overline{w}}}\rho^w\mathbf{g}^{\overline{w}}+\overset{w\to s}{\mathbf{T}}]\cdot\mathbf{v}^{\overline{w}}=\Lambda\geqslant 0, \quad (17)$$

where θ is the temperature, $\mathbf{I}$ is the identity tensor, p^w is the macroscale fluid pressure, $\mathbf{d}^{\overline{\overline{w}}}$ is the macroscale rate of strain tensor defined as

$$\mathbf{d}^{\overline{\overline{w}}}=\tfrac{1}{2}[\nabla\mathbf{v}^{\overline{w}}+(\nabla\mathbf{v}^{\overline{w}})^{\mathrm{T}}], \quad (18)$$

$\mu^{\overline{w}}$ is the chemical potential, $\psi^{\overline{w}}$ is the gravitational potential, and Λ is the entropy production rate density of the system.

Equation (17) is in flux-force form, and it provides permissibility constraints for closure relations. The specific form of closure relations is not unique, but any valid condition must not violate Eq. (17). All members of the set of fluxes are unique and all members of the set of forces are also unique. These properties allow fluxes to be considered one at a time. Closure relations may be posited as either conjugate flux-force or cross-coupled flux-forces in form [60]. The usual approach is to generate the simplest possible form of the closure relations that yields a useful model for the application of concern.

The flux in the first term on the left-hand side of Eq. (17) involves the stress tensor and the fluid pressure, and the conjugate force is the rate of strain tensor. Both the flux and the force vanish at least at equilibrium. One possible closure relation consistent with the entropy inequality is a zero-order closure, such that

$$\mathbf{t}^{\overline{\overline{w}}}=-p^w\mathbf{I}\,. \quad (19)$$

This closure approximation is a statement that the flow is inviscid at the macroscale. This is reasonable if momentum transfer between the fluid and solid phase dominates over the interaction of the fluid with a boundary of the system. Given the typically large interfacial area between the fluid and solid phase compared to the interfacial area between the fluid and the boundary of most domains of interest, this closure approximation is not only simple but also well founded [60].

The second term on the left-hand side of Eq. (17) describes the entropy production due to the flow of the fluid through the medium, and its interaction with the solid phase. A simple closure relation consistent with the second law of thermodynamics and a known production of entropy resulting from flow is a first-order conjugate flux-force closure of the form

$$\epsilon^{\overline{\overline{w}}}\nabla p^w-\epsilon^{\overline{\overline{w}}}\rho^w\nabla(\mu^{\overline{w}}+\psi^{\overline{w}})-\epsilon^{\overline{\overline{w}}}\rho^w\mathbf{g}^{\overline{w}}+\overset{w\to s}{\mathbf{T}}=\hat{\mathbf{R}}^w\cdot\mathbf{v}^{\overline{w}}, \quad (20)$$

where $\hat{\mathbf{R}}^w$ is a second-rank positive definite resistance tensor, where quantities with hats denote material parameters. This form ensures that any flow generates entropy. The axiom of objectivity in continuum mechanics requires all velocities to be relative velocities, but in this case the relative

velocity is assumed to be the solid-phase velocity, which is zero in the reference coordinate system as a result of the secondary restrictions.

Equation (20) contains a chemical potential, gravitational potential, and momentum transfer that must be manipulated to produce a solvable model. Each of these terms will need to be calculated from more readily available quantities. Additionally, Eq. (20) does not include viscosity, so it is not yet apparent how the viscous effects of GNFs will impact the resistance.

The chemical potential may be calculated using the macroscale Gibbs-Duhem equation for a steady-state, isothermal system [[60], Eq. (7.33)]:

$$-\epsilon^{\overline{w}}\nabla p^{w} + \epsilon^{\overline{w}}\rho^{w}\nabla\mu^{\overline{w}} - \langle\nabla(p_w - p^{w})\rangle_{\Omega_w,\Omega} + \langle\rho_w\nabla(\mu_w - \mu^{\overline{w}})\rangle_{\Omega_w,\Omega} = 0, \tag{21}$$

which as a result of secondary restrictions (8) and (10) may be written as

$$-\epsilon^{\overline{w}}\nabla p^{w} + \epsilon^{\overline{w}}\rho^{w}\nabla\mu^{\overline{w}} = 0, \tag{22}$$

and the gravitational potential may be calculated by averaging [[60], Eq. (2.50)], using the gradient theorem from [[60], Eq. (B.13)], which gives

$$\epsilon^{\overline{w}}\rho^{w}\nabla\psi^{\overline{w}} = -\epsilon^{\overline{w}}\rho^{w}\mathbf{g}^{\overline{w}} - \epsilon^{\overline{ws}}\langle\rho_w\psi_w\mathbf{n}_w\rangle_{\Omega_{ws},\Omega_{ws}}\,. \tag{23}$$

The momentum transfer is defined in-terms of averaged microscale quantities by [[60], Eq. (6.83)]

$$\overset{w\to s}{\mathbf{T}} = -\langle[\mathbf{t}_w + \rho_w(\mathbf{v}_w - \mathbf{v}_w^{\overline{ws}})(\mathbf{v}_{ws} - \mathbf{v}_w)]\cdot\mathbf{n}_w\rangle_{\Omega_{ws},\Omega}, \tag{24}$$

where $\mathbf{n}_w$ is the outward normal of the w phase, secondary restrictions (4), (5), (7), and (8) have lead to a jump condition for momentum transfer from the fluid to the solid phase, and ws indicates the fluid-solid interface. The velocity product term is related to mass transfer, which does not occur in this system, allowing Eq. (24) to be written as

$$\overset{w\to s}{\mathbf{T}} = -\langle\mathbf{t}_w\cdot\mathbf{n}_w\rangle_{\Omega_{ws},\Omega}. \tag{25}$$

The microscale stress tensor for an isotropic, incompressible GNF is [60]

$$\mathbf{t}_w = -p_w\mathbf{I} + 2\hat{\mu}_w\mathbf{d}_w\,. \tag{26}$$

Substituting Eq. (26) into Eq. (25) gives

$$\overset{w\to s}{\mathbf{T}} = \epsilon^{\overline{ws}}\langle p_w\mathbf{n}_w\rangle_{\Omega_{ws},\Omega_{ws}} - \epsilon^{\overline{ws}}\langle 2\hat{\mu}_w\mathbf{d}_w\cdot\mathbf{n}_w\rangle_{\Omega_{ws},\Omega_{ws}}. \tag{27}$$

Substituting Eqs. (22), (23), and (27) into Eq. (20) and rearranging yields

$$\epsilon^{\overline{ws}}\langle\rho_w\psi_w\mathbf{n}_w\rangle_{\Omega_{ws},\Omega_{ws}} + \epsilon^{\overline{ws}}\langle p_w\mathbf{n}_w\rangle_{\Omega_{ws},\Omega_{ws}} - \epsilon^{\overline{ws}}\langle 2\hat{\mu}_w\mathbf{d}_w\cdot\mathbf{n}_w\rangle_{\Omega_{ws},\Omega_{ws}} = \hat{\mathbf{R}}^{w}\cdot\mathbf{v}^{\overline{w}}, \tag{28}$$

which shows the role of dynamic viscosity in the calculation of resistance, and may be used to introduce the GNF rheological model.

E. Darcy's Law

It has been shown that Darcy's law may be written as [59,60,79,80]

$$\mathbf{q}^{\overline{w}} = -\frac{\hat{\mathbf{K}}^{w}}{g}\cdot\nabla(\mu^{\overline{w}} + \psi^{\overline{w}}), \tag{29}$$

where $\hat{\mathbf{K}}^{w}$ is a symmetric, second-rank, positive semidefinite hydraulic conductivity tensor, and g is the gravitational acceleration constant. We wish to connect Eq. (29) to results derived using the above TCAT analysis in the Newtonian fluid limit.

Applying secondary restriction (6) to Eq. (16) and substituting Eq. (19) for the stress tensor yields

$$-\nabla(\epsilon^{\overline{\overline{w}}}p^w) + \epsilon^{\overline{\overline{w}}}\rho^w\mathbf{g}^{\overline{w}} = {}^{w\rightarrow s}\mathbf{T}, \tag{30}$$

which may be combined with Eq. (20) giving

$$-\nabla(\epsilon^{\overline{\overline{w}}}p^w) + \epsilon^{\overline{\overline{w}}}\nabla p^w - \epsilon^{\overline{\overline{w}}}\rho^w\nabla(\mu^{\overline{w}} + \psi^{\overline{w}}) = \hat{\mathbf{R}}^w \cdot \mathbf{v}^{\overline{w}}. \tag{31}$$

substituting Eqs. (22) and (23) into Eq. (31) and applying secondary restriction (8) yields

$$-\epsilon^{\overline{\overline{w}}}\nabla p^w + \epsilon^{\overline{\overline{w}}}\rho^w\mathbf{g}^{\overline{w}} + \epsilon^{\overline{\overline{ws}}}\langle\rho_w\psi_w\mathbf{n}_w\rangle_{\Omega_{ws},\Omega_{ws}} = \hat{\mathbf{R}}^w \cdot \mathbf{v}^{\overline{w}}. \tag{32}$$

Multiplying through by $\epsilon^{\overline{\overline{w}}}$, recalling that

$$\mathbf{q}^{\overline{\overline{w}}} = \epsilon^{\overline{\overline{w}}}\mathbf{v}^{\overline{w}} \tag{33}$$

yields

$$\mathbf{q}^{\overline{\overline{w}}} = -\epsilon^{\overline{\overline{w}}^2}(\hat{\mathbf{R}}^w)^{-1} \cdot \left(\nabla p^w - \rho^w\mathbf{g}^{\overline{w}} - \frac{\epsilon^{\overline{\overline{ws}}}}{\epsilon^{\overline{\overline{w}}}}\langle\rho_w\psi_w\mathbf{n}_w\rangle_{\Omega_{ws},\Omega_{ws}}\right). \tag{34}$$

At equilibrium, it follows that

$$0 = \nabla p^w - \rho^w\mathbf{g}^{\overline{w}} - \frac{\epsilon^{\overline{\overline{ws}}}}{\epsilon^{\overline{\overline{w}}}}\langle\rho_w\psi_w\mathbf{n}_w\rangle_{\Omega_{ws},\Omega_{ws}}. \tag{35}$$

It has previously been proven that at equilibrium for a similar system that [[81], Eq. (45)]

$$0 = \nabla p^w - \rho^w\mathbf{g}^{\overline{w}} + \frac{\epsilon^{\overline{\overline{ws}}}}{\epsilon^{\overline{\overline{w}}}}\langle(p_w - p^w)\mathbf{n}_w\rangle_{\Omega_{ws},\Omega_{ws}}, \tag{36}$$

which as a result of secondary restriction (8) reduces to

$$0 = \nabla p^w - \rho^w\mathbf{g}^{\overline{w}} + \frac{\epsilon^{\overline{\overline{ws}}}}{\epsilon^{\overline{\overline{w}}}}\langle p_w\mathbf{n}_w\rangle_{\Omega_{ws},\Omega_{ws}}. \tag{37}$$

Equations (35) and (37) may be equated to yield a condition that holds at equilibrium

$$\langle(\rho_w\psi_w + p_w)\mathbf{n}_w\rangle_{\Omega_{ws},\Omega_{ws}} = 0. \tag{38}$$

The relationship between Darcy's law and the above averaged TCAT formulation can be observed by equating the RHS of Eqs. (29) and (34):

$$\frac{\hat{\mathbf{K}}^w}{g} \cdot \nabla(\mu^{\overline{w}} + \psi^{\overline{w}}) = \epsilon^{\overline{\overline{w}}^2}(\hat{\mathbf{R}}^w)^{-1} \cdot \left(\nabla p^w - \rho^w\mathbf{g}^{\overline{w}} - \frac{\epsilon^{\overline{\overline{ws}}}}{\epsilon^{\overline{\overline{w}}}}\langle\rho_w\psi_w\mathbf{n}_w\rangle_{\Omega_{ws},\Omega_{ws}}\right). \tag{39}$$

Hydraulic conductivity may be written for Newtonian fluids in terms of intrinsic permeability and viscosity as

$$\hat{\mathbf{K}}^w = \frac{\hat{\mathbf{k}}^w\rho^w g}{\hat{\mu}^w}, \tag{40}$$

where $\hat{\mathbf{k}}^w$ is the intrinsic permeability [82,83]. Plugging the above, Eqs. (22) and (23) into Eq. (39) gives

$$\frac{\hat{\mathbf{k}}^w}{\hat{\mu}^w} = \epsilon^{\overline{\overline{w}}^2}(\hat{\mathbf{R}}^w)^{-1}. \tag{41}$$

With Eq. (41), it is possible to convert between the resistance derived using TCAT and intrinsic permeability for the Newtonian limit.

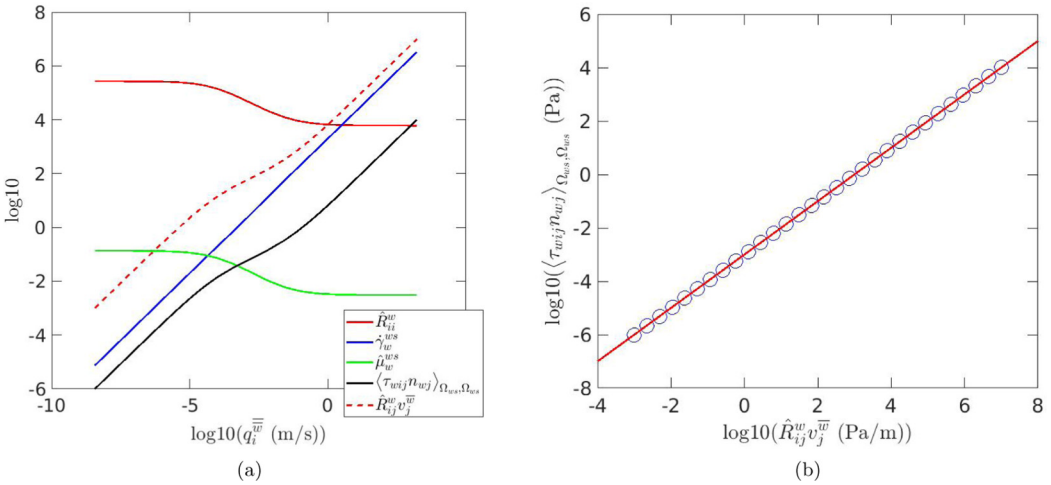

FIG. 2. Parallel slit flow: (a) magnitudes of relevant terms in Eq. (28); and (b) comparison of normalized terms.

Equation (29) formulates Darcy's law in terms of gravitational and chemical potential, which is more precise than the traditional mathematical representations of Darcy's law, which are written in terms of hydraulic head [82]. Equation (41) may be used to relate Darcy's law, within the TCAT framework, to hydraulic resistance. Hydraulic resistance is a linear scaling factor that relates the force-per-volume applied by the fluid to the solid phase to the fluid-phase velocity, as may be observed from Eq. (28).

IV. GENERALIZED NEWTONIAN FLUID RESISTANCE

For the Newtonian fluid case with conditions specified in the secondary restrictions, $\hat{\mathbf{R}}^{w}$ is constant and independent of flow conditions. This condition is not the case for GNF's, even for the constant porosity, Stokes flow case considered herein. The focus in the literature on shift-factor approaches indicates that a function for resistance exists that depends upon the rheological form of the GNF [10,11,30,40,41]; however, these empirical approaches have not been connected to the microscale physics of flow through a porous medium. The purpose of this section is to investigate GNF flow through two different porous media using a microscale computational approach and use the insights gained from these computational experiments to develop a general closure approximation for macroscale models in the Stokes flow limit. More specifically, flow of Fluid 3 summarized in Table I was simulated through the parallel slits and the BCC media described in Sec. II. This fluid was selected because the entirety of Cross model behavior occurs before transition effects away from Stokes flow become significant. Flow in the parallel slits case was purely pressure driven, while in the BCC case flow was purely body-force driven.

A. Resistance data

The parallel slits geometry was selected because an analytical solution for Cross model flow is available, and because the first two terms in Eq. (28) are negligible for this case. Using Einstein notation and defining the viscous stress tensor as $\tau_{wij} = 2\hat{\mu}_w d_{wij}$, the analytical results for $\langle \tau_{wij} n_{wj} \rangle_{\Omega_{ws},\Omega_{ws}}$, $\hat{\mu}_w^{ws}$, $\dot{\gamma}_w^{ws}$, $\hat{R}_{ii}^{w}$, and $\hat{R}_{ij}^{w} v_j^{\overline{w}}$ are shown in Fig. 2(a) for a set of flow simulations. In Fig. 2(b) $\langle \tau_{wij} n_{wj} \rangle_{\Omega_{ws},\Omega_{ws}}$ is plotted as a function of $\hat{R}_{ij}^{w} v_j^{\overline{w}}$, with a linear trendline incorporated into the figure. It is apparent from Fig. 2(a) that $\hat{\mu}_w^{ws}$ is of a similar shape as $\hat{R}_{ii}^{w}$ and that $\dot{\gamma}_w^{ws}$ is

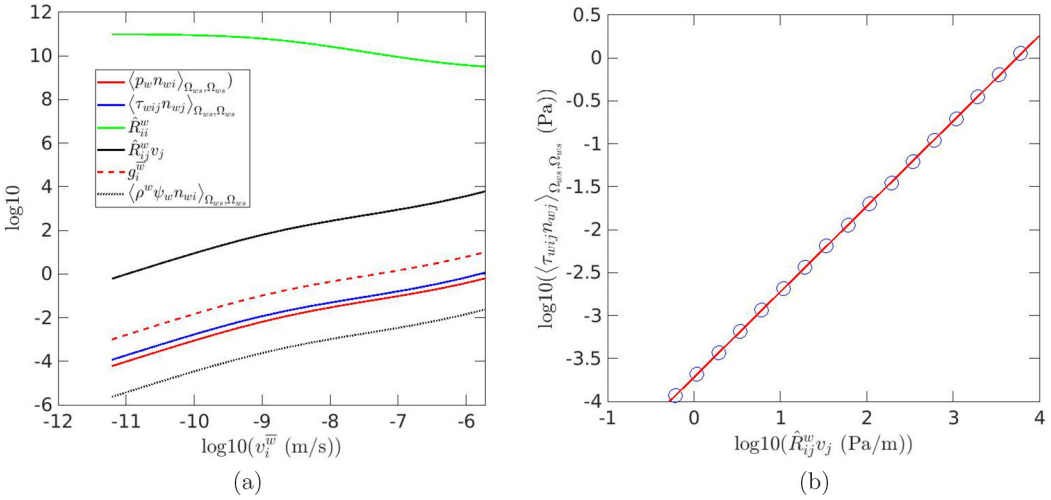

FIG. 3. BCC flow: (a) magnitudes of relevant terms in Eq. (28); and (b) comparison of normalized terms.

log-linearly related to $q_i^{\overline{\overline{w}}}$ for this case. Figure 2(b) shows that $\langle \tau_{wij} n_{wj} \rangle_{\Omega_{ws},\Omega_{ws}}$ is a linear function of $\hat{R}_{ii}^{w} v_i^{\overline{w}}$.

The BCC system geometry was selected because it is a relatively simple geometry for which the first two terms in Eq. (28) are significant. The same quantities plotted in Fig. 2(a) are shown for the BCC case in Fig. 3(a) as a function of $v_i^{\overline{w}}$ with $g_i^{\overline{w}}$, $\langle \rho_w \psi_w n_{wi} \rangle_{\Omega_{ws},\Omega_{ws}}$ and $\langle p_w n_{wi} \rangle_{\Omega_{ws},\Omega_{ws}}$ also included. Figure 3(b) shows $\langle \tau_{wij} n_{wj} \rangle_{\Omega_{ws},\Omega_{ws}}$ as a function of $\hat{R}_{ij}^{w} v_j^{\overline{w}}$ with a linear trendline, as in the slit case. The data for the BCC case shows similar characteristics to the slits case. The data presented here will inform our model formulation in the next section.

B. Resistance analysis

Based on the data presented above for a Cross model fluid, we posit that $\log \hat{R}_{ii}^{w}$ will depend upon $\log q_i^{\overline{\overline{w}}}$, and that Newtonian behavior will be observed in both the limit of relatively small and large $\mathbf{q}^{\overline{\overline{w}}}$, albeit with different $\hat{\mu}^{w}$ in each limit that corresponds to $\hat{\mu}_0$ and $\hat{\mu}_\infty$, respectively. The upper limit on $q_i^{\overline{\overline{w}}}$ must still be within the Stokes regime, although this limit may not exist for some Cross model parameter choices. We are concerned with the case in which the upper limit does exist. The resistance limits will be defined as $\hat{\mathbf{R}}_0^{w}$ and $\hat{\mathbf{R}}_\infty^{w}$, where the subscripts 0 and ∞ correspond to the lower and upper dynamic viscosity limit conditions, respectively. The Newtonian resistance limits may be connected to Darcy's law using Eq. (39).

It is clear that a transition must exist in $\hat{\mathbf{R}}^{w}$ between the two Newtonian limits. Based on Figs. 2(b) and 3(b), we posit that this transition is of a similar form to the Cross model, which can be written as

$$\hat{R}_{ii}^{w} = \hat{R}_{\infty ii}^{w} + \frac{\hat{R}_{0ii}^{w} - \hat{R}_{\infty ii}^{w}}{1 + \left(M_i q_i^{\overline{\overline{w}}}\right)^n}, \tag{42}$$

where M_i is a constant that is related to m in the Cross model.

It can be observed from Figs. 2(b) and 3(b) that the inflection point of the log of the resistance occurs at a similar flow rate as the inflection point of the log of $\langle 2\hat{\mu}_w \mathbf{d}_w \cdot \mathbf{n}_w \rangle_{\Omega_{ws},\Omega_{ws}}$, a value that may be calculated by a macroscale analogy to the microscale Cross model. Because the nonlinear scaling between asymptotic limits in both Eqs. (2) and (42) occurs because of the denominators, we

can equate these two terms for the inflection point in $\log \hat{\mu}_w$ and the inflection point in $\log \hat{R}^w_{ii}$ giving

$$M_i = \frac{m\dot{\gamma}_I}{q^{\overline{\overline{w}}}_{Ii}}, \tag{43}$$

where $\dot{\gamma}_I$ is the inflection point shear rate, which may be calculated directly from the Cross model, and $q^{\overline{\overline{w}}}_{Ii}$ is the ith component of the inflection point Darcy velocity. If $q^{\overline{\overline{w}}}_{Ii}$ can be computed analytically, then it is clear that $\hat{R}^w_{ii}$ can be deduced with only knowledge of the Newtonian behavior and the Cross model parameters without the need to carry out simulations or experiments for any GNF fluid.

To calculate $\mathbf{q}^{\overline{\overline{w}}}_I$, a few assumptions must be made. First, it will be assumed that at $\mathbf{q}^{\overline{\overline{w}}}_I$,

$$|\langle 2\hat{\mu}_w(d_{wij}n_{wj})\rangle_{\Omega_{ws},\Omega_{ws}}| \approx \hat{\mu}_I\dot{\gamma}_I, \tag{44}$$

where

$$\hat{\mu}_I = \sqrt{\hat{\mu}_0\hat{\mu}_\infty}. \tag{45}$$

Similarly to the inflection point viscosity, the inflect point resistance components are

$$\hat{R}^w_{Iii} = \sqrt{\hat{R}^w_{\infty ii}\hat{R}^w_{0\,ii}}. \tag{46}$$

It is shown in Figs. 2(b) and 3(b) that

$$-\langle 2\hat{\mu}_w\mathbf{d}_w\cdot\mathbf{n}_w\rangle_{\Omega_{ws},\Omega_{ws}} = \hat{\mathbf{L}}^w\cdot\hat{\mathbf{R}}^w\cdot\mathbf{v}^{\overline{w}}, \tag{47}$$

where $\hat{\mathbf{L}}^w$ is some length scale. Figures 2(b) and 3(b) shows that $\hat{\mathbf{L}}^w$ is insensitive to velocity, indicating that this scaling tensor may be calculated for a medium when a Newtonian fluid flows through it and tabulated for that medium similarly to the intrinsic permeability and resistance. The above assumption implies that a similar linear relationship could also be posed for the sum of the first two terms in Eq. (28); however, linear relationships for each of those individual terms can be shown to only arise in specific circumstances.

Using Eq. (47), as well as the assumption present in Eq. (44), to calculate $\mathbf{q}^{\overline{\overline{w}}}_I$ gives the components

$$q^{\overline{\overline{w}}}_i = \frac{\epsilon^{\overline{\overline{w}}}\sqrt{\hat{\mu}_0\hat{\mu}_\infty}\dot{\gamma}_I}{\hat{L}^w_{ii}\sqrt{\hat{R}^w_{0\,ii}\hat{R}^w_{\infty ii}}}. \tag{48}$$

Substituting the above into Eq. (43) gives

$$M_i = \frac{m\hat{L}^w_{ii}\sqrt{\hat{R}^w_{0\,ii}\hat{R}^w_{\infty ii}}}{\epsilon^{\overline{\overline{w}}}\sqrt{\hat{\mu}_0\hat{\mu}_\infty}}. \tag{49}$$

With the above calculations, all parameters needed to predict GNF can be computed from a Newtonian flow experiment and the Cross model rheological parameters by calculating:

(i) the velocity and pressure field for a known driving force made up of ∇p^w and/or $\mathbf{g}^{\overline{w}}$,
(ii) averaged values for $\langle\rho_w\psi_w\mathbf{n}_w\rangle_{\Omega_{ws},\Omega_{ws}}$ and $\langle p_w\mathbf{n}_w\rangle_{\Omega_{ws},\Omega_{ws}}$,
(iii) scaling factor, $\hat{\mathbf{L}}$, using Eq. (47),
(iv) $\hat{\mathbf{R}}^w$ for the Newtonian flow using Eq. (32),
(v) $\hat{\mathbf{R}}^w_0$ and $\hat{\mathbf{R}}^w_\infty$ using the Newtonian $\hat{\mathbf{R}}^w$ and scaling by viscosity, and
(vi) M_i using Eq. (49) with $\hat{\mathbf{L}}$ calculated above, and $\hat{\mathbf{R}}^w_I$ from Eq. (46).

With the parameters determined *a priori*, the resistance for GNF fluids can be computed without the need to carry out any additional experiments.

In a case where only macroscale data is available, such as in laboratory experiments, the direct computation of averaged microscale quantities would not be accessible. Two approaches are possible for this case. First, flow data for one GNF could be used to determine q_{Ii} corresponding to

$\hat{R}^w_{Iii}$ and $\hat{\mathbf{L}}^w$ could be computed using Eqs. (44) and (47). While this would require experimental data from flow of one GNF, this $\hat{\mathbf{L}}^w$ may be tabulated and used to predict flow of other GNFs, similarly to how the intrinsic permeability is used to predict flow of Newtonian fluids. Second, GNF flow data would not be required if $\hat{\mathbf{L}}^w$ was known. Since this length scale is related to the pore morphology and topology, estimations of this tensor could be derived based upon measures of the pore structure, such as the Sauter mean diameter, the statistics of the grain size distribution, the porosity, the specific interfacial area of the solid phase, and perhaps other accessible measures. Because these length scale correction terms are higher order terms, it is expected that a reasonable approximation of $\hat{\mathbf{L}}^w$ would be sufficient.

C. TCAT GNF approximation summary

The resistance tensor, which is regularly used in macroscale modeling, was shown to be related to the average shear stress of the fluid at the ws-interface using TCAT. A method to use the macroscale formulation was then used to show how to derive an *a priori* resistance function for Cross model fluids.

Several assumptions have been made during the development of this theory that are in addition to the secondary restrictions described in Sec. III A, and which may be summarized:

(i) $\dot{\gamma}_w \approx 2|\mathbf{d}_w \cdot \mathbf{n}_w|$, as in Eq. (44);

(ii) $\hat{R}^w_{ii}$ is a function of $q_i^{\overline{\overline{w}}}$ with a similar form to whichever GNF model is of interest, as in Eq. (42);

(iii) the log of $\hat{R}^w_{ii}$ has an inflection point that occurs at the same flow rate as the log of $\hat{\mu}_w$;

(iv) the pressure and gravitational potential acting on the ws-interface, from Eq. (28), is linearly proportional to the average shear-stress at the ws-interface, as in Eq. (47); and

(v) the anisotropic case may be approximated using $\hat{R}^w_{ii}$ and $q_i^{\overline{\overline{w}}}$.

Each of these assumptions may be investigated either individually or collectively using microscale simulations. Results and analysis from the application of the derived formulation to a variety of test cases is considered in the following section.

V. MODEL EVALUATION AND VALIDATION

The validation of the theory derived here was performed using five different GNFs (Table I) and four different media: (1) three parallel slits; (2) flow through a periodic BCC unit cell of spheres; (3) flow in a system of polydisperse packed spheres; and (4) flow through a periodic BCE unit cell (Tables II–IV). OpenFOAM simulations of GNF flow through each domain were carried out as described in Sec. II, with microscale data being averaged using Paraview and averaging utilities built into OpenFOAM. Flow rates were selected such that flow was within the Stokes regime. $\hat{\mathbf{R}}^w$ was calculated using Eq. (28) with the averaged microscale data output from simulations. $\hat{\mathbf{R}}^w$ and $\hat{\mathbf{L}}$ were calculated for a Newtonian fluid case using Eqs. (28) and (47), respectively. A predicted $\hat{\mathbf{R}}^w$ was calculated using Eq. (42) with the *a priori* parameters described above, including in Eq. (49). The predicted $\hat{\mathbf{R}}^w$ was then compared to the values observed from numerical simulation. It was assumed that an average relative error in R_{ii} between predicted and observed values of $\leqslant 2\%$ would validate the *a priori* approach, as this would be within the expected numerical error for the simulations. The parameters calculated for each medium are included in Table V.

It is common practice to treat a porous medium either as a bundle of capillary tubes, or in some cases as a set of parallel slits [1,9,10,82]. This is generally done because analytical solutions can often be derived for these simple geometries, and because such systems represent simple instances of a porous medium system. For the parallel slit medium, the pressure and potential normal averaged terms can be neglected, providing a simple test case. This system is ideal for comparison to the *a priori* model because it explicitly excludes transition or turbulent flow behavior and the solution is analytically computed, thus any error between the predicted and observed behavior must be due to model approximations.

TABLE V. Parameters calculated from simulation of Newtonian flow through each domain with a dynamic viscosity of $\hat{\mu}_w = 0.001$ Pa s, and a density $\rho_w = 1000$ kg/m^3.

Parameter	Parallel Slits	BCC	Packed Spheres	BCE
$\hat{\mathbf{R}}^w_{11}$ (Pa s/m^2)	2×10^3	1.17×10^5	1.25×10^6	1.07×10^5
$\hat{\mathbf{R}}^w_{22}$ (Pa s/m^2)		1.17×10^5	1.25×10^6	4.65×10^4
$\hat{\mathbf{R}}^w_{33}$ (Pa s/m^2)		1.17×10^5	1.25×10^6	5.57×10^4
$\hat{\mathbf{L}}_{11}$ (m)	1×10^{-3}	1.89×10^{-4}	3.61×10^{-5}	1.70×10^{-4}
$\hat{\mathbf{L}}_{22}$ (m)		1.89×10^{-4}	3.61×10^{-5}	3.07×10^{-4}
$\hat{\mathbf{L}}_{33}$ (m)		1.89×10^{-4}	3.61×10^{-5}	3.19×10^{-4}
$\epsilon^{\overline{\overline{ws}}}$ (m^2/m^3)	1×10^3	3.41×10^3	1.80×10^4	2.43×10^3

The results of the *a priori* resistance relationship compared to observed results for the parallel slits case are shown in Fig. 4(a). The average error of the predicted resistance relative to the observed resistance was generally less than 1%, with the largest average error being 1.25% for Fluid 2.

The second case investigated was a periodically arranged BCC unit cell arrangement of a set of spheres. Potential normal averages were expected to be nonnegligible for this case. $\hat{\mathbf{L}}$ was calculated during each simulation to check the validity of the assumption that it was a constant that is a characteristic of the medium. Calculation of the *a priori* parameters used required one single Newtonian simulation to characterize the medium.

A comparison of the predicted and observed $\hat{R}^w$ for the BCC medium is shown in Fig. 4(b). The observed error was similar to that observed with the parallel slit case and consistently less than 1%. $\hat{\mathbf{L}}$ was found to vary less than 1% with the biggest changes noted in the regions immediately before and after the inflection point in the resistance for each fluid. The observed error in the predicted $\hat{\mathbf{R}}^w$ was similar to the numerical error in this quantity found from a grid refinement study.

A packed set of spheres was investigated to further evaluate the GNF resistance model for a more complicated flow system than afforded by the parallel slit and BCC cases considered. Fluids 3 and 5 were simulated so that the full range of GNF behavior could be observed without significant inertial effects. A polydisperse sphere packing was selected to investigate whether the single length scale assumption presented in Eq. (47) still holds. While this system is not large enough to be considered a representative elementary volume for randomly packed spheres [84], the theory should still apply. $\hat{\mathbf{L}}$ was checked for each simulation and again was found to change less than 1%. The TCAT model is compared to the observed resistance in Fig. 4(c). The average error was less than 2%, again within the expected numerical error.

Ellipsoids with principal directions aligned with the directions of flow were selected so that the resistance model could be evaluated for an anisotropic medium, which has received scant attention for GNF flow using any approach [85–87]. Fluids 3 and 4 were simulated flowing in each of the principal directions of the medium. Simulation of a Newtonian fluid flowing in each principal direction was undertaken to calculate the Newtonian permeability and $\hat{\mathbf{L}}$. The results for the two fluids may be seen in Figs. 4(d) and 4(e). The average relative error between the predicted and observed resistances for each fluid in each dimension did not exceed 1%. Simulations of flow that was unaligned with the principal directions of the coordinate system were undertaken by adjusting the body force components driving flow; these results were predicted from the aligned flow analysis with an average error that was less than 1%.

VI. DISCUSSION

The results show that the TCAT approximation to describe GNF flow through porous media derived in Sec. III accurately models a variety of systems and GNFs. Two other approaches typically used to model GNFs at the macroscale are idealized pore-scale models [4,30,40,46,88–92] and

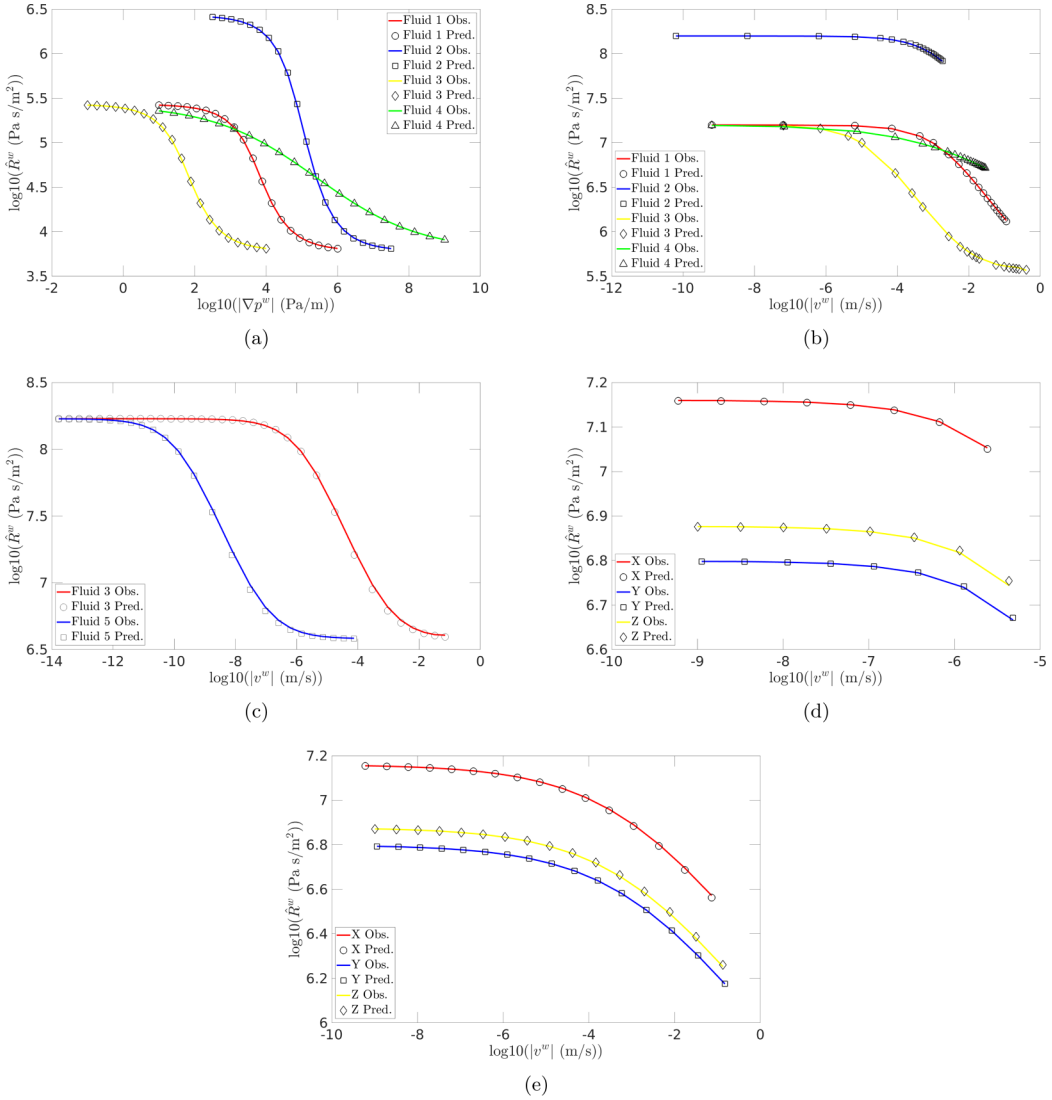

FIG. 4. Simulation results for: (a) a set of parallel slits; (b) BCC array of spheres; (c) randomly packed sphere domain; (d) BCE array of ellipsoids for Fluid 3; and (e) BCE array of ellipsoids for Fluid 4.

the shift-factor approach coupled with Darcy's law [10,11,30,40,41,86,93–95]. The purpose of this section is to compare the TCAT method developed in this work with these traditional methods.

Bundle of capillary tubes and pore-network models both use idealized pore-scale geometries to directly calculate flow [4,30,40,46,88–92], and often center on modifying the Ergun [41,46,47,92] or Carman-Kozeny [50] equations phenomenologically to approximate GNF flow behavior. The bundle of capillary tubes approach does not include a precise representation of the true interconnection among pores and the actual pore structure of natural porous medium systems [4,82,83,96,97]. Pore-network models approximate the interconnection among pores, but this method still uses an idealized approximation of real media, making it sub-optimal when modeling a typical porous medium system [98–100]. Despite the limitations associated with idealization of the pore structure, both the bundle of capillary tubes and pore-network models can approximate pore-scale GNF flow

using analytical microscale solutions that can be integrated to the macroscale. For GNFs, idealized pore-scale models are used to calculate shift factors [30,40,46,88,91,92]. Because shift factors are still the goal of such simulations, the primary focus here will be to compare the resistance model derived with the traditional shift-factor approach.

The shift factor, sometimes called the shape factor [30,40,46], is an empirical factor typically implemented to approximate the GNF flow for isotropic systems [10,11,30,40,41], with limited anisotropic applications appearing in the literature [86,93–95]. The traditional approach is to use the shift factor to calculate an effective viscosity, which is used in Darcy's law in place of a constant Newtonian viscosity [10,11,30,40,41,86,93–95].

The TCAT approach advanced in this work connects microscale physics with macroscale representations and advances an improved approach for modeling macroscale systems. The insight gained from the TCAT formulation can be used to analyze the shift-factor approach. Using Eq. (41) for the isotropic case, and replacing the viscosity with the effective viscosity, gives

$$\frac{\hat{k}^w}{\hat{\mu}^{\overline{\overline{w}}}_{\text{eff}}} = \epsilon^{\overline{\overline{w}}2}(\hat{R}^w)^{-1}. \tag{50}$$

Rearranging Eq. (50), using Eqs. (2) and (42), and assuming that the microscale Cross model may be written in terms of effective parameters at the macroscale gives

$$\frac{\hat{k}^w}{\epsilon^{\overline{\overline{w}}2}}\left[\hat{R}^w_\infty + \frac{\hat{R}^w_0 - \hat{R}^w_\infty}{1 + (\hat{M}q^{\overline{\overline{w}}})^n}\right] = \hat{\mu}^w_\infty + \frac{\hat{\mu}^w_0 - \hat{\mu}^w_\infty}{1 + (m\dot{\gamma}^{\overline{\overline{w}}}_{\text{eff}})^n}. \tag{51}$$

Calculating $\hat{R}^w_\infty$ and $\hat{R}^w_0$ using Eq. (41) and rearranging yields

$$\hat{M}q^{\overline{\overline{w}}} = m\dot{\gamma}^{\overline{\overline{w}}}_{\text{eff}}. \tag{52}$$

Substituting Eqs. (3) and (49) into Eq. (52), calculating the Newtonian limit resistances as above, and rearranging reveals the relationship between the shift factor and the characteristic length $\hat{L}^w$,

$$\hat{\alpha} = \hat{L}^w\sqrt{\frac{\epsilon^{\overline{\overline{w}}3}}{\hat{k}^w}}. \tag{53}$$

Equation (53) links the traditional shift factor approach to the resistance model derived here, and may be used to determine how $\hat{\mu}^{\overline{\overline{w}}}_{\text{eff}}$ relates to averaged microscale quantities. This is done by returning to Eq. (50) and calculating the resistance using Eq. (47), which in scalar form gives

$$\frac{\hat{k}^w}{\hat{\mu}^{\overline{\overline{w}}}_{\text{eff}}} = \epsilon^{\overline{\overline{w}}2}\frac{\hat{L}^w v^{\overline{w}}}{|-\langle 2\hat{\mu}_w \mathbf{d}_w \cdot \mathbf{n}_w\rangle_{\Omega_{ws},\Omega_{ws}}|}. \tag{54}$$

Converting $v^{\overline{w}}$ to $q^{\overline{\overline{w}}}$, calculating $q^{\overline{\overline{w}}}$ from Eq. (3), and rearranging yields

$$\hat{k}^w|-\langle 2\hat{\mu}_w \mathbf{d}_w \cdot \mathbf{n}_w\rangle_{\Omega_{ws},\Omega_{ws}}| = \frac{1}{\hat{\alpha}}\epsilon^{\overline{\overline{w}}}\hat{L}^w\sqrt{\epsilon^{\overline{\overline{w}}}\hat{k}^w}\hat{\mu}^{\overline{\overline{w}}}_{\text{eff}}\dot{\gamma}^{\overline{\overline{w}}}_{\text{eff}}. \tag{55}$$

Substituting Eq. (53) into Eq. (55) and simplifying results in

$$|-\langle 2\hat{\mu}_w \mathbf{d}_w \cdot \mathbf{n}_w\rangle_{\Omega_{ws},\Omega_{ws}}| = \hat{\mu}^{\overline{\overline{w}}}_{\text{eff}}\dot{\gamma}^{\overline{\overline{w}}}_{\text{eff}}, \tag{56}$$

which links the effective variables used in the shift-factor approach to averaged microscale quantities.

The TCAT approach has been used to derive an approach for modeling GNF flow through anisotropic porous media at the macroscale that can be based on only the rheological characterization of a Cross-model fluid, the permeability of the medium for a Newtonian fluid, and an estimate of $\hat{\mathbf{L}}^w$. Furthermore, we have used these results to shed new light on the shift-factor approach by relating $\hat{\alpha}$ to the new TCAT formulation and shown the averaged microscale expression that is approximated implicitly by effective macroscale parameters.

VII. CONCLUSIONS

A new theory that directly links the dynamic viscosity for a Cross model fluid to the hydraulic resistance was proposed for Stokes, single-phase fluid flow in porous medium systems. The theory showed that the average viscosity at the fluid-solid interface is a primary parameter that impacts Stokes flow at the macroscale. The theory developed also shows that two additional forces that act on the fluid-solid interface, which are typically neglected, may be significant when predicting the hydraulic resistance during GNF flow. These two forces are the average normal pressure, and the average normal gravitational potential that are acting on the fluid-solid interface.

The insights gained from averaging within the TCAT framework were used when investigating flow of a GNF through multiple media. It was found that the viscous forces acting on the fluid-solid interface are linearly proportional to the fluid velocity, and that this constant of proportionality can be calculated from flow data for one fluid. The relationship between resistance and flow rate was found to be similar to the relationship between viscosity and shear rate for Cross model fluids, and a functional form was derived. The equations relating dynamic viscosity to resistance were used to derive parameters for the GNF resistance approximation that may be calculated *a priori* using only a Newtonian flow characterization and the rheology of the GNF.

The newly proposed model was related to the popular shift factor approach, and it was shown how effective viscosity and shear rate may be related to averaged microscale quantities. The proposed model is an improvement on the shift factor approach for modeling GNF flow because it does not require flow experiments through porous media for GNF fluids, all assumptions have been clearly identified, and it applies to both isotropic and anisotropic cases. The resistance calculated from the proposed model was typically within 1% of the observed value on average, consistent with the numerical error of the simulations.

ACKNOWLEDGMENTS

This work was supported by National Science Foundation Grant No. 1604314, Army Research Office Grant No. W911NF1920270, and National Institute of Environmental Health Sciences Grant No. P42ES031007. W. G. Gray and T. M. Weigand provided useful discussion related to this work.

[1] A. Skelland, *Non-Newtonian Flow and Heat Transfer* (John Wiley and Sons, New York, 1967).
[2] F. A. Morrison, *Understanding Rheology* (Oxford University Press, Oxford, UK, 2001).
[3] R. B. Bird, W. E. Stewart, and E. N. Lightfoot, *Transport Phenomena*, 2nd ed. (Wiley, New York, 2002).
[4] T. Sochi, Non-Newtonian flow in porous media, Polymer **51**, 5007 (2010).
[5] M. M. Cross, Rheology of non-Newtonian fluids: A new flow equation for pseudoplastic systems, J. Colloid Sci. **20**, 417 (1965).
[6] D. V. Boger, Demonstration of upper and lower Newtonian fluid behavior in a pseudoplastic fluid, Nature (London) **265**, 126 (1977).
[7] V. Subbaraman, R. A. Mashelkar, and J. Ulbrecht, Extrapolation procedures for zero shear viscosity with a falling sphere viscometer, Rheol. Acta **10**, 429 (1971).
[8] R. P. Chhabra and P. H. T. Uhlherr, Estimation of zero-shear viscosity of polymer solutions from falling sphere data, Rheol. Acta **18**, 593 (1979).
[9] T. Sochi, Analytical solutions for the flow of Carreau and Cross fluids in circular pipes and thin slits, Rheol. Acta **54**, 745 (2015).
[10] M. Zhang, M. Prodanovic, M. Mirabolghasemi, and J. Zhao, 3D microscale flow simulation of shear-thinning fluids in a rough fracture, Transp. Porous Media **128**, 243 (2019).
[11] S. C. Hauswirth, C. A. Bowers, C. P. Fowler, P. B. Schultz, A. Dye Hauswirth, T. M. Weigand, and C. T. Miller, Modeling cross model non-Newtonian fluid flow in porous media, J. Contam. Hydrol. **235**, 103708 (2020).

[12] M. Peyrounette, Y. Davit, M. Quintard, and S. Lorthois, Multiscale modelling of blood flow in cerebral microcirculation: Details at capillary scale control accuracy at the level of the cortex, PLoS One **13**, e0189474 (2018).
[13] N. Bessonov, A. Sequira, S. Simakov, Y. Vassilevskii, and V. Volpert, Methods of blood flow modelling, Math. Modell. Nat. Phenom. **11**, 1 (2016).
[14] K. Sriram, M. Intaglietta, and D. M. Tartakovksy, Non-Newtonian flow of blood in aterioles: Consequences for wall shear stress measurements, Microcirculation **21**, 628 (2014).
[15] S. Chakraborty, Dynamics of capillary flow of blood into a microfluidic channel, Lab Chip **5**, 421 (2005).
[16] M. Rabby, A. Razzak, and M. M. Molla, Pulsatile non-Newtonian blood flow through a model of arterial stenosis, Procedia Eng. **56**, 225 (2013).
[17] J. A. F. Gerrard, M. F. Perutz, A. Roch, and G. I. Taylor, Measurement of the velocity distribution along a vertical line through a glacier, Proc. R. Soc. A **213**, 546 (1952).
[18] C. Ancey and M. Meunier, Estimating bulk rheological properties of flowing snow avalanches from field data, J. Geophys. Res. **109**, F01004 (2004).
[19] C. Ancey, Plasticity and geophysical flows: A review, J. Non-Newtonian Fluid Mech. **142**, 4 (2007).
[20] A. C. Barr, R. T. Pappalardo, and S. Zhong, Convective instability in ice I with non-Newtonian rheology: Application to the icy Galilean satellites, J. Geophys. Res. **109**, E12008 (2004).
[21] G. Hulme, The interpretation of lava flow morphology, Geophys. J. Int. **39**, 361 (1974).
[22] Y. S. Wu, An approximate analytical solution for non-Darcy flow toward a well in fractured media, Water Resour. Res. **38**, 1023 (2002).
[23] I. Sonder, B. Zimanowski, and R. Buttner, Non-Newtonian viscosity of basaltic magma, Geophys. Res. Lett. **33** (2006).
[24] E. Lev, M. Spiegelman, R. J. Wysocki, and J. A. Karson, Investigating lava flow rheology using video analysis and numerical flow models, J. Volcanol. Geotherm. Res. **247-248**, 62 (2012).
[25] A. A. Osiptsov, Fluid mechanics of hydraulic fracturing: A review, J. Pet. Sci. Eng. **156**, 513 (2017).
[26] W. Norman, R. Jasinski, and E. Nelson, Hydraulic fracturing process and compositions, U.S. Patent No. 5,551,516 (1996).
[27] R. Barati and J.-T. Liang, A review of fracturing fluid systems used for hydraulic fracturing of oil and gas wells, J. Appl. Polym. Sci. **131** (2014).
[28] A. C. Barbati, J. Desroches, A. Robisson, and G. H. McKinley, Complex fluids and hydraulic fracturing, Annu. Rev. Chem. Biomol. Eng. **7**, 415 (2016).
[29] C. Xie, W. Lv, and M. Wang, Shear-thinning or shear-thickening fluid for better EOR? A direct pore-scale study, J. Pet. Sci. Eng. **161**, 683 (2018).
[30] C. L. Perrin, P. M. J. Tardy, K. S. Sorbie, and J. C. Crawshaw, Experimental and modeling study of Newtonian and non-Newtonian fluid flow in pore network micromodels, J. Colloid Interface Sci. **295**, 542 (2006).
[31] T. C. Buchley and D. L. Lord, What to learn about hydraulic fracturing fluids, Oil Gas J. **71**, 84 (1973).
[32] J. Chen and X. Lu, Numerical investigation of the non-Newtonian pulsatile blood flow in a bifurcation model with a nonplanar branch, J. Biomech. **39**, 818 (2006).
[33] J. Mejia, R. Mongrain, and O. F. Bertrand, Accurate prediction of wall shear stress in a stented artery: Newtonian versus non-Newtonian models, J. Biomech. Eng. **133**, 074501 (2011).
[34] M. I. Billen and G. Hirth, Newtonian versus non-Newtonian upper mantle viscosity: Implications for subduction initiation, Geophys. Res. Lett. **32**, L19304 (2005).
[35] P. R. S. Mendes, Dimensionless non-Newtonian fluid mechanics, J. Non-Newtonian Fluid Mech. **147**, 109 (2007).
[36] R. L. Thompson and E. J. Soares, Viscoplastic dimensionless numbers, J. Non-Newtonian Fluid Mech. **238**, 57 (2016).
[37] P. D. M. Spelt, T. Selerland, C. J. Lawrence, and P. D. Lee, Flows of inelastic non-Newtonian fluids through arrays of aligned cylinders. part 1. creeping flows, J. Eng. Math. **51**, 57 (2005).
[38] P. Coussot, Yield stress fluid flows: A review of experimental data, J. Non-Newtonian Fluid Mech. **211**, 31 (2014).

[39] D. Bauer, L. Talon, Y. Peysson, H. B. Ly, G. Batot, T. Chevalier, and M. Fleury, Experimental and numerical determination of Darcy's law for yield stress fluids in porous media, Phys. Rev. Fluids **4**, 063301 (2019).
[40] K. S. Sorbie, P. J. Clifford, and E. R. W. Jones, The rheology of pseudoplastic fluids in porous media using network modeling, J. Colloid Interface Sci. **130**, 508 (1989).
[41] T. Tosco, D. L. Marchisio, and F. Lince, Extension of the Darcy-Forchheimer law for shear-thinning fluids and validation via pore-scale flow simulations, Transp. Porous Media **96**, 1 (2013).
[42] T. J. Sadowshi and R. B. Bird, Non-Newtonian flow through porous media I. Theoretical, Trans. Soc. Rheol. **9**, 243 (1965).
[43] G. Chauveteau, Rodlike polymer solution flow through fine pores: Influence of pore size on rheological behavior, J. Rheol. **26**, 111 (1982).
[44] R. Parnas and Y. Cohen, Power-law fluids in porous media, Chem. Eng. Commun. **53**, 3 (1987).
[45] R. E. Hayes, A. Afacan, B. Boulanger, and A. V. Shenoy, Modelling the flow of power law fluids in a packed bed using a volume-averaged equation of motion, Transp. Porous Media **23**, 175 (1996).
[46] S. Liu and J. H. Masliyah, Non-linear flows in porous media, J. Non-Newtonian Fluid Mech. **86**, 229 (1999).
[47] A. R. Castro and G. Radilla, Non-Darcian flow of shear-thinning fluids through packed beads: Experiments and predictions using Forchheimer's law and Ergun's equation, Adv. Water Resour. **100**, 35 (2017).
[48] S. Berg and J. Wunnik, Shear rate determination from pore-scale flow fields, Transp. Porous Media **117**, 229 (2017).
[49] N. Zamani, I. Bondino, R. Kaufmann, and A. Skauge, Computation of polymer *in situ* rheology using direct numerical simulation, J. Pet. Sci. Eng. **159**, 92 (2017).
[50] A. R. Castro, Extending Darcy's law to the flow of yield stress fluids in packed beds: Method and experiments, Adv. Water Resour. **126**, 55 (2019).
[51] F. Zami-Pierre, R. de Loubens, M. Quintard, and Y. Davit, Transition in the Flow of Power-Law Fluids Through Isotropic Porous Media, Phys. Rev. Lett. **117**, 074502 (2016).
[52] M. K. Hubbert, Darcy's law and the field equations of the flow of underground fluids, Trans. Amer. Inst. Min. Eng. **207**, 222 (1956).
[53] W. G. Gray and K. O'Neill, On the development of Darcy's law for the general equations for flow in porous media, Water Resour. Res. **12**, 148 (1976).
[54] S. P. Neuman, Theoretical derivation of Darcy's Law, Acta Mech. **25**, 153 (1977).
[55] S. Whitaker, Flow in porous media I: A theoretical derivation of Darcy's law, Transp. Porous Media **1**, 3 (1986).
[56] J. M. Nordbotten, M. A. Celia, H. K. Dahle, and S. M. Hassanizadeh, Interpretation of macroscale variables in Darcy's law, Water Resour. Res. **43**, W08430 (2007).
[57] W. G. Gray, C. T. Miller, and B. A. Schrefler, Response to comment on "Averaging theory for description of environmental problems: What have we learned?" Adv. Water Resour. **52**, 331 (2013).
[58] J. P. Singh, S. Padhy, E. S. G. Shaqfeh, and D. L. Koch, Flow of power-law fluids in fixed beds of cylinders or spheres, J. Fluid Mech. **713**, 491 (2012).
[59] W. G. Gray and C. T. Miller, Thermodynamically constrained averaging theory approach for modeling flow and transport phenomena in porous medium systems: 3. Single-fluid-phase flow, Adv. Water Resour. **29**, 1745 (2006).
[60] W. G. Gray and C. T. Miller, *Introduction to the Thermodynamically Constrained Averaging Theory for Porous Medium Systems* (Springer, Switzerland, 2014).
[61] C. T. Miller and W. G. Gray, Thermodynamically constrained averaging theory approach for modeling flow and transport phenomena in porous medium systems: 4. Species transport fundamentals, Adv. Water Resour. **31**, 577 (2008).
[62] W. G. Gray and C. T. Miller, Thermodynamically constrained averaging theory approach for modeling flow and transport phenomena in porous medium systems: 5. Single-fluid-phase transport, Adv. Water Resour. **32**, 681 (2009).

[63] W. G. Gray and C. T. Miller, Thermodynamically constrained averaging theory approach for modeling flow and transport phenomena in porous medium systems: 7. Single-phase megascale flow models, Adv. Water Resour. **32**, 1121 (2009).
[64] A. S. Jackson, C. T. Miller, and W. G. Gray, Thermodynamically constrained averaging theory approach for modeling flow and transport phenomena in porous medium systems: 6. Two-fluid-phase flow, Adv. Water Resour. **32**, 779 (2009).
[65] W. G. Gray, A. L. Dye, J. E. McClure, L. J. Pyrak-Nolte, and C. T. Miller, On the dynamics and kinematics of two-fluid-phase flow in porous media, Water Resour. Res. **51**, 5365 (2015).
[66] I. V. Rybak, W. G. Gray, and C. T. Miller, Modeling two-fluid-phase flow and species transport in porous media, J. Hydrol. **521**, 565 (2015).
[67] C. T. Miller, W. G. Gray, C. E. Kees, I. V. Rybak, and B. J. Shepherd, Modeling sediment transport in three-phase surface water systems, J. Hydraul. Res. **57**, 439 (2019).
[68] G. Sciumé, S. E. Shelton, W. G. Gray, C. T. Miller, F. Hussain, M. Ferrari, P. Decuzzi, and B. A. Schrefler, Tumor growth modeling from the perspective of multiphase porous media mechanics, Mol. Cell. Biomech. **9**, 193 (2012).
[69] G. Sciumé, S. Shelton, W. G. Gray, C. T. Miller, F. Hussain, M. Ferrari, P. Decuzzi, and B. A. Schrefler, A multiphase model for three-dimensional tumor growth, New J. Phys. **15**, 015005 (2013).
[70] C. T. Miller, W. G. Gray, and B. A. Schrefler, A continuum mechanical framework for modeling tumor growth and treatment in two- and three-phase systems, Arch. Appl. Mech. (2021), doi: 10.1007/s00419-021-01891-8.
[71] S. R. Williams and A. P. Philipse, Random packings of spheres and spherocylinders simulated by mechanical contraction, Phys. Rev. E **67**, 051301 (2003).
[72] J. Riegel, W. Mayer, and Y. van Havre, Freecad, https://www.freecadweb.org/.
[73] L. S. Caretto, A. D. Gosman, S. V. Patankar, and D. B. Spalding, Two calculation procedures for steady, three-dimensional flows with recirculation, in *Proceedings of the 3rd International Conference on Numerical Methods in Fluid Mechanics*, edited by H. Cabannes and R. Temam, Vol. 19 (Springer, Berlin, Heidelberg, 1973), p. 60.
[74] C. Greenshields, *OpenFOAM User Guide version 6* (OpenFOAM Foundation, London, 2018).
[75] U. Ayachit, *The ParaView Guide Community Edition* (Kitware, New York, NY, 2019).
[76] M. Icardi, G. Boccardo, D. L. Marchisio, T. Tosco, and R. Sethi, Pore-scale simulation of fluid flow and solute dispersion in three-dimensional porous media, Phys. Rev. E **90**, 013032 (2014).
[77] C. T. Miller and W. G. Gray, Thermodynamically constrained averaging theory approach for modeling flow and transport phenomena in porous medium systems: 2. Foundation, Adv. Water Resour. **28**, 181 (2005).
[78] C. T. Miller, F. J. Valdés-Parada, and B. D. Wood, A pedagogical approach to the thermodynamically constrained averaging theory, Transport Porous Meda **119**, 585 (2017).
[79] W. G. Gray and C. T. Miller, TCAT analysis of capillary pressure in nonequilibrium, two-fluid-phase, porous medium systems, Adv. Water Resour. **34**, 770 (2011).
[80] W. G. Gray and C. T. Miller, A generalization of averaging theorems for porous medium analysis, Adv. Water Resour. **62**, 227 (2013).
[81] W. G. Gray and C. T. Miller, On the algebraic and differential forms of Darcy's equation, J. Porous Media **14**, 33 (2011).
[82] J. Bear, *Dynamics of Fluids in Porous Media* (Elsevier, New York, 1972).
[83] G. de Marsily, *Quantitative Hydrogeology: Groundwater Hydrology for Engineers* (Academic Press, San Diego, CA, 1986).
[84] C. Pan, M. Hilpert, and C. T. Miller, Pore-scale modeling of saturated permeabilities in random sphere packings, Phys. Rev. E **64**, 066702 (2001).
[85] A. Fadili, P. M. J. Tardy, and J. R. A. Pearson, A 3D filtration law for power-law fluids in heterogeneous porous media, J. Non-Newtonian Fluid Mech. **106**, 121 (2002).
[86] L. Orgeas, Z. Idris, C. Geindreau, J.-F. Bloch, and J.-L. Auriault, Modelling the flow of power-law fluids through anisotropic porous media at low-pore Reynolds number, Chem. Eng. Sci. **61**, 4490 (2006).

[87] V. Di Federico, M. Pinelli, and R. Ugarelli, Estimates of effective permeability for non-Newtonian fluid flow in randomly heterogeneous porous media, Stoch. Environ. Res. Risk Assess. **24**, 1067 (2010).
[88] J. R. A. Pearson and P. M. J. Tardy, Models for flow of non-Newtonian and complex fluids through porous media, J. Non-Newtonian Fluid Mech. **102**, 447 (2002).
[89] C. N. Basset, M. R. Abou Najm, A. Ammar, R. D. Stewart, S. C. Hauswirth, and G. Saad, Physically based model for extracting dual-permeability parameters using non-Newtonian fluids, Vadose Zone J. **18**, 1 (2019).
[90] S. C. Hauswirth, M. R. Abou Najm, and C. T. Miller, Characterization of the pore structure of porous media using non-Newtonian fluids, Water Resources Research **55**, 7182 (2019).
[91] H. E. Fayed, N. A. Sheikh, and O. Iliev, On laminar flow of non-Newtonian fluids in porous media, Trans. Porous Media **111**, 253 (2016).
[92] N. Kaur, R. Singh, and R. K. Wanchoo, Flow of Newtonian and non-Newtonian fluids through packed beds: An experimental study, Trans. Porous Media **90**, 655 (2011).
[93] L. Orgéas, C. Geindreau, J. L. Auriault, and J. F. Bloch, Upscaling the flow of generalised Newtonian fluids through anisotropic porous media, J. Non-Newtonian Fluid Mech. **145**, 15 (2007).
[94] J. K. Woods, P. D. M. Spelt, P. D. Lee, T. Selerland, and C. J. Lawrence, Creeping flows of power-law fluids through periodic arrays of elliptical cylinders, J. Non-Newtonian Fluid Mech. **111**, 211 (2003).
[95] L. Patacchini and R. de Loubens, A class of physically stable non-linear models of flow through anisotropic porous media, Trans. Porous Media **97**, 409 (2013).
[96] I. Fatt, The network model of porous media: I. Capillary pressure characteristics, Trans. AIME **207**, 144 (1956).
[97] S. Erol, S. J. Fowler, V. Harcouet-Menou, and B. Laenen, An analytical model of porosity-permeability for porous and fractured media, Trans. Porous Media **120**, 327 (2017).
[98] Q. Xiong, T. G. Baychev, and A. P. Jivkov, Review of pore network modelling of porous media: Experimental characterisations, network constructions and applications to reactive transport, J. Cont. Hydrology **192**, 101 (2016).
[99] T. Sweijen, S. M. Hassanizadeh, B. Chareyre, and L. Zhuang, Dynamic pore-scale model of drainage in granular porous media: The pore-unit assembly method, Water Res. Research **54**, 4193 (2018).
[100] H. Adloo and B. Abbasi, Some insights into the use of pore network simulations for predicting single-phase fluid flow in model porous media, Microfluid. Nanofluid. **25**, 61 (2021).